Variable density and viscosity, miscible displacements in horizontal Hele-Shaw cells. Part 1. Linear stability analysis

L. Talon[1,2], **N. Goyal**[2] **and E. Meiburg**[2],†

[1]Laboratoire Fluides Automatique et Systèmes Thermiques, Universités P. et M. Curie, CNRS
(UMR 7608) Bâtiment 502, Campus Universitaire, 91405 Orsay Cedex, France

[2]Department of Mechanical Engineering, University of California, Santa Barbara, CA 93106, USA

A computational investigation of variable density and viscosity, miscible displacements in horizontal Hele-Shaw cells is presented. As a first step, two-dimensional base states are obtained by means of simulations of the Stokes equations, which are nonlinear due to the dependence of the viscosity on the local concentration. Here, the vertical position of the displacement front is seen to reach a quasisteady equilibrium value, reflecting a balance between viscous and gravitational forces. These base states allow for two instability modes: first, there is the familiar tip instability driven by the unfavourable viscosity contrast of the displacement, which is modulated by the presence of density variations in the gravitational field; second, a gravitational instability occurs at the unstably stratified horizontal interface along the side of the finger. Both of these instability modes are investigated by means of a linear stability analysis. The gravitational mode along the side of the finger is characterized by a wavelength of about one half to one full gap width. It becomes more unstable as the gravity parameter increases, even though the interface is shifted closer to the wall. The growth rate is largest far behind the finger tip, where the interface is both thicker, and located closer to the wall, than near the finger tip. The competing influences of interface thickness and wall proximity are clarified by means of a parametric stability analysis. The tip instability mode represents a gravity-modulated version of the neutrally buoyant mode. The analysis shows that in the presence of density stratification its growth rate increases, while the dominant wavelength decreases. This overall destabilizing effect of gravity is due to the additional terms appearing in the stability equations, which outweigh the stabilizing effects of gravity onto the base state.

Key words: buoyancy-driven instability, fingering instability, Hele-Shaw flows

---

1. Introduction

The displacement of a more viscous fluid by a less viscous one in a Hele-Shaw cell represents a fundamental problem that has been studied from many points of view,

† Email address for correspondence: meiburg@engineering.ucsb.edu
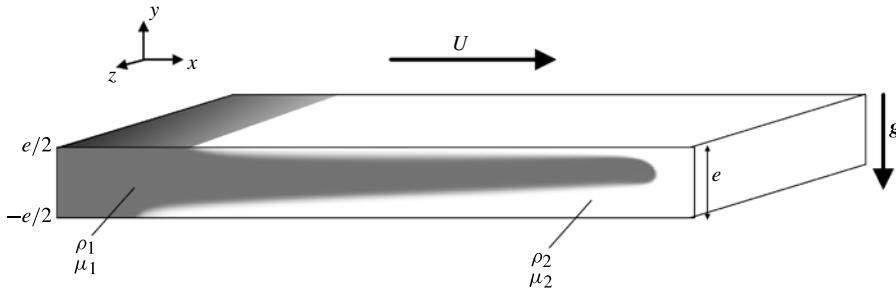
FIGURE 1. Configuration of a horizontal Hele-Shaw displacement. The lighter and less viscous fluid 1 injected from the left displaces the denser, more viscous resident fluid 2 to the right.

cf. the reviews by Homsy (1987) and Yortsos & Zeybek (1988). In recent years, a number of investigations have focused on the miscible variant of this flow, in order to assess the role of diffusion and dispersion (Taylor 1953) in displacement processes. The unfavourable viscosity contrast usually causes these flows to be unstable (Goyal & Meiburg 2006), although this instability is frequently modulated by the simultaneous existence of density variations.

When the displacement direction is aligned with the direction of gravity (Wooding 1969; Lajeunesse *et al.* 1997), the main symmetry of the flow with regard to the centre plane of the gap is maintained in the presence of a density difference. Nevertheless, these density differences can lead to a substantial change in the dominant wavelength and the associated growth rate (Lajeunesse *et al.* 1999; Goyal, Pichler & Meiburg 2007). Related information for the corresponding Darcy problem is provided by Bacri, Rakotomalala & Salin (1991) and Manickam & Homsy (1993). On the other hand, when a variable density displacement occurs in a predominantly horizontal direction (cf. figure 1), the interplay between viscosity and density stratification can be fundamentally different, as gravity will now destroy the up–down symmetry of the base flow within the gap of the Hele-Shaw cell. The flow has the form of a finger of the less viscous fluid propagating along the centre of cell, while layers of the resident, more viscous fluid are left behind on the walls. More recently, Taghavi and coauthors (Taghavi *et al.* 2009, 2010, 2011, 2012) have extended such investigations to address the role of channel inclination and inertial forces in displacement flows. Furthermore, several authors have addressed displacement flows in horizontal capillary tubes (Chen & Meiburg 1996; Petitjeans & Maxworthy 1996; Vanaparthy & Meiburg 2008; Martin *et al.* 2011) as well as in inclined tubes (Séon *et al.* 2004, 2005, 2006, 2007a,b).

In addition, the situation of unidirectional base flows with viscosity and density differences, and the instabilities that can arise in such flows, has been investigated by a number of authors (Govindarajan 2004; Selvam *et al.* 2007; d'Olce *et al.* 2008, 2009; Sahu *et al.* 2009a,b; Selvam *et al.* 2009). For unidirectional flows in the absence of density variations, the linear stability investigation by Talon & Meiburg (2011) showed that three-layer, miscible Poiseuille flows can be unstable even in the Stokes flow limit. In the presence of a density difference, one of the horizontal interfaces will be gravitationally unstable, while the other one is stable. In this context, we note that Maxworthy (2004, personal communication) has experimentally observed longitudinal 'streaks' superimposed on growing viscous fingers, which may indicate the presence of a secondary instability. These streaks are aligned in the displacement direction,

and they are separated in the spanwise direction by a distance that is several times shorter than the wavelength of the viscous fingering instability. Similar observations of additional flow structures were made in the parabolic flight experiments by Vedernikov *et al.* (2001) and Aubertin *et al.* (2009), as a result of the transition from microgravity to amplified gravity of nearly twice the normal strength. To the best of the authors' knowledge, neither the features of the base flow in the presence of a density difference, nor the origin of these longitudinal streaks have been addressed to date, either theoretically or computationally. The present investigation aims to analyse this flow configuration based on the three-dimensional Stokes equations. Towards this end, we will first establish the nature of the two-dimensional base flow in the gap of the cell as a function of the governing dimensionless parameters. Subsequently, we will linearize the three-dimensional equations around this two-dimensional base state, in order to analyse its stability characteristics.

Section 2 will define the physical problem, state the governing equations, and provide a brief overview over the numerical methods employed. By means of Stokes simulation results, § 3 will discuss the influence of gravitational effects on the two-dimensional base flow in the gap. Subsequently, § 4 investigates the potential for a gravitational instability to develop along the predominantly horizontal interfaces of this base state. A parametric stability analysis will serve to clarify the roles of interfacial thickness and wall proximity. Section 5 discusses the modulation of the viscously driven tip instability by gravity. The two instability modes are compared in terms of their respective growth rates and wavelengths in § 6, and a summary of the findings is presented. In Part 2 (John *et al.* 2013), we will extend the present linear stability investigation to nonlinear simulations, in order to address the role of density differences in viscously unstable, miscible displacements (Oliveira & Meiburg 2011).

2. Problem formulation

2.1. *Governing equations*

Figure 1 displays the flow configuration in a horizontal Hele-Shaw cell of width e. A lighter and less viscous fluid 1 is injected from the left with an average velocity U, thereby displacing the resident, heavier and more viscous fluid 2 to the right. The two fluids are miscible with each other in all proportions. Here z and x denote the spanwise and main flow directions, respectively. Gravitational forces, which act in the cross-gap $-y$-direction, result in the loss of symmetry with regard to the centre plane of the Hele-Shaw cell, as they cause the lighter, injected fluid to rise upwards. Since the no-slip condition at the upper wall causes a thin layer of the heavier, resident fluid to remain next to the wall, a gravitationally unstable interface forms on the upper side of the injected fluid that may give rise to a gravitational instability. The present investigation aims to analyse this density-driven instability namely the viscously driven instability at the finger tip, and to identify the respective parameter regimes dominated by each of them.

We focus on situations in which density differences are small and a suitably formed Reynolds number typically is less than $O(1)$. The flow field then satisfies the three-dimensional incompressible Navier–Stokes equations under the Boussinesq approximation, along with a convection–diffusion equation for the concentration field

$$\nabla \cdot \boldsymbol{u} = 0, \qquad (2.1)$$

$$\rho_2 \left(\frac{\partial \boldsymbol{u}}{\partial t} + \boldsymbol{u}\nabla\boldsymbol{u} \right) = -\nabla(p + \rho_2 gy) + \nabla \cdot \tau + (\rho - \rho_2)\boldsymbol{g}, \qquad (2.2)$$

$$\frac{\partial c}{\partial t} + \boldsymbol{u} \cdot \nabla c = D \Delta c. \tag{2.3}$$

Here $\boldsymbol{u}$ denotes the fluid velocity vector, while τ indicates the Newtonian stress tensor. Here p, ρ and c refer to pressure, density and concentration of the displaced fluid, respectively, and $\boldsymbol{g}$ represents the vector of gravitational acceleration. The diffusion coefficient D is taken to be constant. As in previous investigations, we assume the density–concentration and viscosity–concentration relationships are linear and exponential, respectively,

$$\rho(c) = \rho_1 + c \Delta \rho, \tag{2.4}$$

$$\mu(c) = \mu_2 \, e^{R(c-1)}, \tag{2.5}$$

with

$$\Delta \rho = \rho_2 - \rho_1, \tag{2.6}$$

$$R = \ln(\mu_2/\mu_1). \tag{2.7}$$

In order to non-dimensionalize the governing equations, we introduce the characteristic scales

$$L^* = e, \quad U^* = U, \quad T^* = \frac{e}{U}, \quad P^* = \frac{\mu_2 U}{e}, \quad \tau^* = \frac{\mu_2 U}{e}. \tag{2.8}$$

We thus obtain for the dimensionless variables $\tilde{\boldsymbol{u}}$, $\tilde{p}$, $\tilde{\rho}$, $\tilde{\tau}$ and c

$$\nabla \cdot \tilde{\boldsymbol{u}} = 0, \tag{2.9}$$

$$Re \left(\frac{\partial \tilde{\boldsymbol{u}}}{\partial \tilde{t}} + \tilde{u} \nabla \tilde{u} \right) = -\nabla \tilde{p} + \nabla \cdot \tilde{\tau} - F \tilde{c} \nabla \tilde{y}, \tag{2.10}$$

$$\frac{\partial c}{\partial \tilde{t}} + \tilde{\boldsymbol{u}} \cdot \nabla c = \frac{1}{Pe} \Delta c, \tag{2.11}$$

with

$$F = \frac{\Delta \rho g e^2}{\mu_2 U}, \tag{2.12}$$

$$Pe = \frac{Ue}{D} \tag{2.13}$$

$$Re = \frac{\rho_2 Ue}{\mu_2}. \tag{2.14}$$

For the sake of simplicity, the tilde symbols will be omitted from now on. The Péclet number Pe indicates the relative magnitudes of the diffusive and convective (based on U) time scales, while the gravity parameter F provides the ratio of buoyancy ($\Delta \rho g$) to viscous ($\mu_2 U/e^2$) forces.

As a result of employing the larger viscosity in rendering the governing equations dimensionless, the Schmidt number $Sc = \nu/D$ of typical fluid combinations ranges from $O(10^4)$ to $O(10^6)$. Hence, even for the largest Péclet numbers of $O(10^3)$ investigated below, a suitably defined Reynolds number is of $O(0.1)$ or less. As is demonstrated in Part 2 (John *et al.* 2013), for such small values of the Reynolds number, the two-dimensional bases states are nearly indistinguishable from their Stokes flow counterparts. For this reason, we employ Stokes flow base states throughout the linear stability investigation. However, in order not to miss any

potential inertially driven instability modes, we keep the inertial terms in the linear stability equations.

2.2. *Numerical implementation*

The numerical implementation follows our previous investigations (Goyal & Meiburg 2004, 2006; Goyal *et al.* 2007), and the reader is referred to these references for detailed information on the solution methodology and convergence checks. In summary, nonlinear simulations of the two-dimensional Stokes equations in the fourth-order streamfunction formulation are employed to obtain the convectively dominated, quasisteady base state in the (x, y)-plane. A typical domain size is $[-6, 6] \times [-0.5, 0.5]$, with a mesh size of 1701×231.

A linear stability analysis of this base state is then performed with regard to spanwise perturbations along the front, and both spanwise and streamwise perturbations along the upper interface. Towards this end, the Stokes equations are linearized around the base state, and subsequently discretized to give a generalized numerical eigenvalue problem. The goal is to determine the eigenvalue

$$\sigma = f(\alpha, \beta, Pe, R, F) \qquad (2.15)$$

representing the growth rate of the perturbation, along with the associated eigenfunctions. The viscosity ratio R, the Péclet number Pe, and the gravity number F all influence the base state separately, and so all three of these dimensionless parameters enter the dispersion relation separately. Here α and β refer to the streamwise and spanwise perturbation wavenumbers, respectively.

The simultaneous presence of gravitational and viscous instabilities, possibly in different regions of the flow field, renders the present situation somewhat more complex as compared with the earlier investigations mentioned above. There, the instability was always limited to the region around the moving tip of the displacement front, even for variable density displacements in vertical Hele-Shaw cells (Goyal *et al.* 2007). Hence, for the linear stability analysis it was sufficient to consider a limited region around the tip, in a reference frame moving with the quasisteady tip velocity, and to assume that the perturbation eigenfunctions would die out away from the tip. In the present situation, on the other hand, we still expect the viscous instability mode to be limited to the tip region, while the gravitational mode can occur anywhere along the upper interface. In this context it is important to realize that the trailing sections of this interface are not advancing with the same quasisteady velocity as the tip, so that their stability properties cannot be investigated in this moving reference frame. Hence, we have to analyse the tip region and the upper interface separately. Additional details will be provided below.

We now proceed to establish and characterize the two-dimensional, quasisteady base states, whose linear stability properties will subsequently be evaluated. Owing to their inherent complexity, these base flows cannot be determined analytically or described in the form of similarity solutions, so that we need to generate them via nonlinear, two-dimensional simulations. This approach had previously been employed successfully by Goyal *et al.* (2007). Here it is important to note that the base flow contains the effects of diffusion, so that it will never become truly steady. However, as we will see, a quasisteady state is established for an extended period of time. In order to conduct the linear stability analysis, we then assume that the time scale on which the base state changes is larger than that which governs the growth of the instability. The validity of this assumption will be established *a posteriori* in Part 2 of this investigation, where we compare the growth rates obtained from present linear stability analysis with those
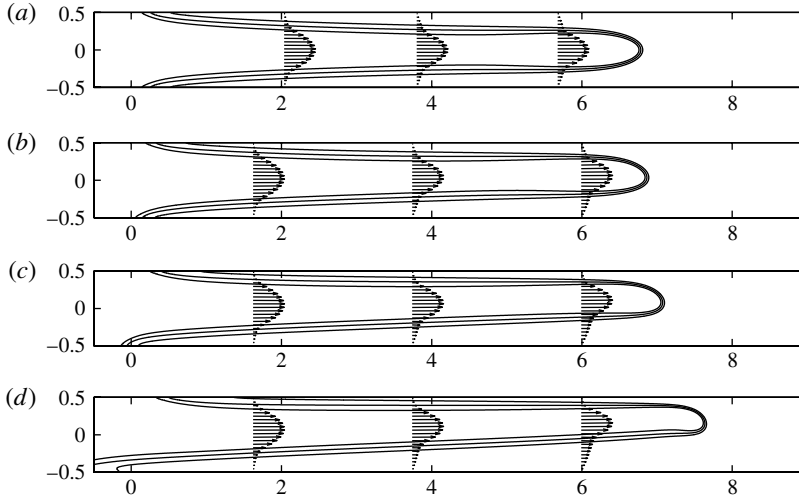
FIGURE 2. Concentration contours $c = 0.1$, 0.5 and 0.9 and some velocity vectors at $t = 4.1$, for two-dimensional displacements with $R = 2.5$ and $Pe = 2000$. The value of the gravity parameter is: (*a*) $F = 0$, (*b*) $F = 40$, (*c*) $F = 60$ and (*d*) $F = 80$. As F increases, the injected, lighter fluid is shifted towards the top of the cell, while the tip propagation velocity of the displacement front increases.

observed in the early stages of fully three-dimensional simulations. This comparison shows that the instability growth during the early stages is captured reasonably well by the linear analysis to be described below.

3. Two-dimensional Stokes flow simulations

The two-dimensional Stokes flow simulations in the x, y-plane are initiated with a Poiseuille flow velocity profile and an error function concentration field

$$c(x, y, t = 0) = \frac{1}{2} + \frac{1}{2}\text{erf}\left(\frac{x}{\delta}\right), \qquad (3.1)$$

where $\delta = 0.1$. As in our earlier investigation of neutrally buoyant displacements (Goyal & Meiburg 2006), the quasisteady flow features and their linear stability properties are independent of δ over a wide range of values. Moreover, the experiments by Aubertin *et al.* (2009) show that the viscous fingering instability occurs only after the formation of the two-dimensional base state, so that the initial interface thickness δ does not influence the properties of the instabilities under consideration.

Figure 2 shows the displacement front (also referred to as 'finger') for various values of the gravitational parameter F, at identical times and for constant values of R and Pe. As expected, for larger F-values the injected, lighter fluid is increasingly shifted towards the top of the cell. Nevertheless, even for large F viscous forces push the tip of the front towards the cell centre, thus resulting in a bending of the displacement front similar to the observations of Petitjeans & Maxworthy (1996) for displacements in capillary tubes.

This shape of the displacement front is reflected in the configuration of the streamlines. Figure 3 displays the streamlines for $R = 2.5$, $F = 80$ and $Pe = 2000$, both in the laboratory reference frame (figure 3*a*) and in the reference frame moving
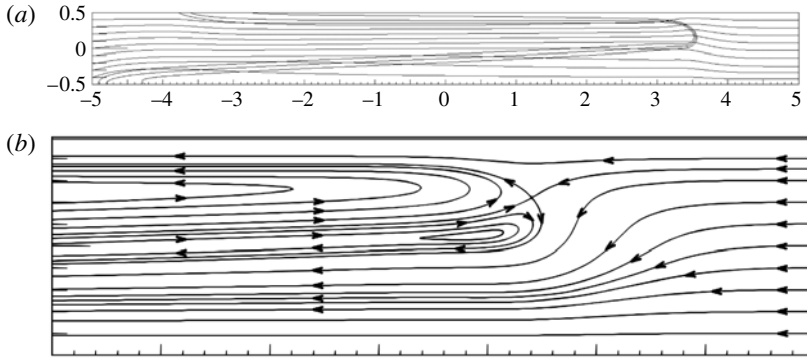
FIGURE 3. Streamlines for the quasisteady base state with $R = 2.5$, $F = 80$ and $Pe = 2000$. (*a*) Streamlines in the laboratory frame of reference. (*b*) Streamlines in the tip region, in the reference frame moving with the tip velocity.
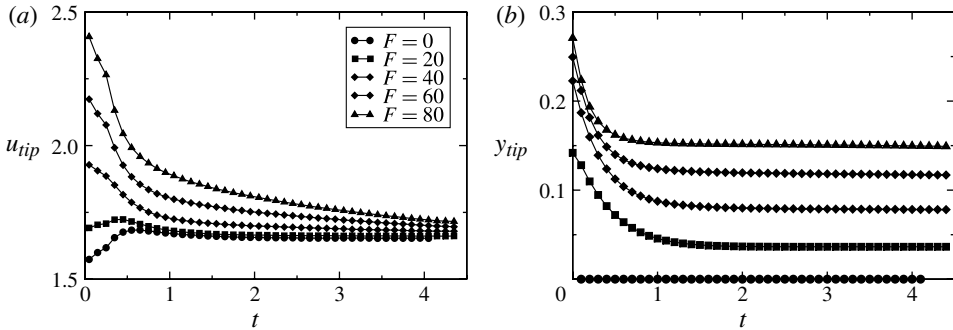
FIGURE 4. Velocity (*a*) and *y*-location (*b*) of the tip as functions of time for different *F*-values, at $R = 2.5$ and $Pe = 2000$. With increasing *F*, the tip propagates faster, and it is located closer to the upper wall.

with the tip (figure 3*b*). Here we define the tip as the farthest downstream position of the $c = 0.5$ contour, located at $(x_{tip}(t), y_{tip}(t))$. The streamlines in the laboratory frame of reference indicate that, within the injected fluid, there is an upward velocity component. Their closer spacing furthermore reflects the fact that within the finger the streamwise velocity is larger than in the corresponding Poiseuille flow regions upstream and downstream of the front. In the moving reference frame, we recognize that the stagnation point near the finger tip has been shifted towards the upper side of the finger by the gravitational forces, and that a small recirculation region has formed in the bottom half of the tip. A more detailed discussion of the long-time evolution of the base state properties can be found in Part 2 (John *et al.* 2013).

Figure 4 displays the evolution of the tip velocity $u_{tip} = dx_{tip}(t)/dt$ and its *y*-position y_{tip} as functions of time. For small *F*, the velocity approaches a steady state after a brief transient, consistent with earlier numerical and experimental observations for $F = 0$ (Chen & Meiburg 1996; Petitjeans & Maxworthy 1996; Rakotomalala, Salin & Watzky 1997*a*,*b*; Goyal & Meiburg 2006). As *F* increases, the transient phase required to establish a quasisteady tip velocity lengthens, until it eventually takes so

long that diffusive effects become noticeable. At this point, a quasisteady tip velocity is no longer observed, although it is interesting that for all F-values the tip velocity eventually converges towards very similar values.

The movement of the tip is governed by the balance of gravitational and viscous forces. While the gravitational forces tend to displace the tip upwards, the viscous forces favour a symmetric flow and, hence, force the tip back towards the centre of the gap. Imagine for a moment that at time $t = 0$, when the interface is vertical, there is no net displacement, so that the flow is driven by density differences only. In this case, the light fluid would rise to the top and form a finger that propagates rightward just below the upper wall. Conversely, the heavy fluid would sink downward and form a left propagating finger along the bottom wall. This mechanism (which corresponds to a viscous lock exchange gravity current, cf. Härtel, Meiburg & Necker (2000)) dominates the very early stages of the flow, so that the tip of the emerging finger initially is far above the centre of the gap. However, soon viscous forces become significant and force the finger tip downward towards the centre of the gap. Hence, the competition between gravitational and viscous forces is responsible for the downward motion of the finger tip during the early phase.

In order to be able to quantify the degree of steadiness of the base state, we employ as a criterion

$$\frac{1}{u_{tip}} \left| \frac{\mathrm{d}u_{tip}}{\mathrm{d}t} \right| < 0.01. \tag{3.2}$$

If this criterion is satisfied, we refer to the base state as quasisteady. Clearly, the allowable value of the tip deceleration represents a somewhat arbitrary parameter in the above criterion. In determining this value, we decided to err on the safe side, i.e. to impose a relatively strict criterion, in order to obtain as 'clean' a base state as possible. It may take a considerable time before the base flow achieves this level of quasisteadiness, and perturbations can, of course, already grow before this state is fully reached. Depending on the initial perturbation level of a three-dimensional simulation or an experiment, it could even be that perturbations will grow to substantial amplitudes before the quasisteady state is fully reached. The experiments by Aubertin *et al.* (2009), however, indicate that the instability usually arises after the quasisteady base state has been reached, thus validating the present approach.

For moderate values of F, the vertical tip location y_{tip} also reaches a quasisteady equilibrium value (figure 4*b*), which confirms that the upward gravitational force acting on the finger is balanced by a corresponding downward viscous force. Interestingly, in spite of its closer proximity to the wall, the transient tip propagation velocity increases with F.

Figure 5 shows the dependence of the tip velocity and its y-position on F, for different viscosity ratios. The tip velocity is seen to increase with F for all values of R. Beyond a certain value of F, a quasisteady state is no longer reached. Consistent with earlier observations for $F = 0$, u_{tip} increases with R for all values of F.

In terms of the present dimensionless variables, the data for the y-location of the tip as function of F are seen to collapse for all values of R, cf. figure 5(*b*). This suggests that only the larger of the two viscosities enters into the equilibrium of gravitational and viscous forces that determines the tip location.

The dependence of u_{tip} and y_{tip} on the Péclet number is shown in figure 6. Consistent with earlier observations for neutrally buoyant displacements, the tip velocity increases with the Péclet number, before levelling off for high *Pe*-values. The *Pe*-value at which this levelling off takes place increases with F. For small *Pe*-values,
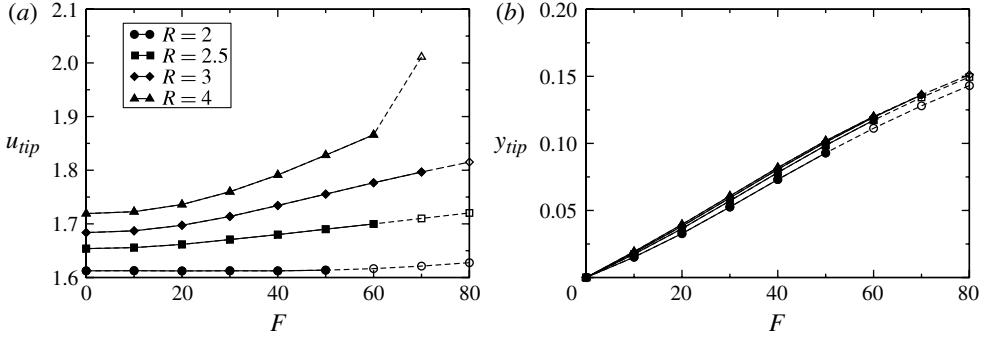
FIGURE 5. Velocity (*a*) and *y*-location (*b*) of the tip as functions of the gravitational parameter *F*, for different viscosity ratios and $Pe = 2000$. Open symbols correspond to simulations where a quasisteady state was not achieved. The curves for the tip location are seen to collapse, which indicates that the equilibrium tip location is not affected by the viscosity ratio.
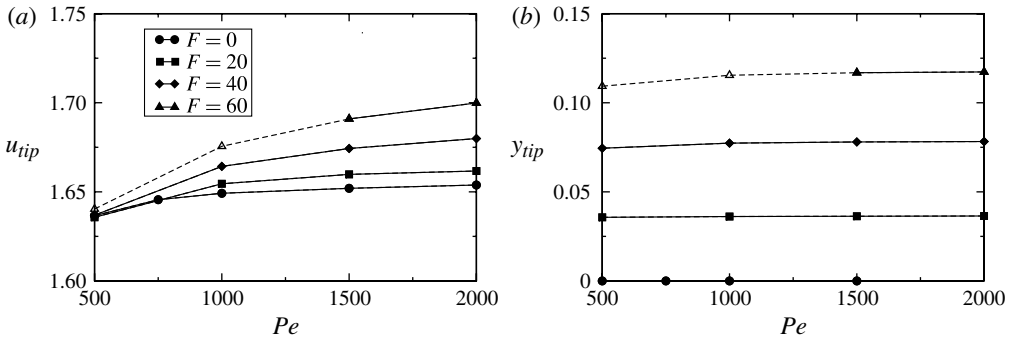
FIGURE 6. Velocity (*a*) and *y*-location (*b*) of the tip as functions of the Péclet number, for different gravity parameters and $R = 2.5$. Open symbols correspond to simulations for which a quasisteady state was not achieved. The tip velocity increases with *Pe* before levelling off, while the tip location is largely independent of *Pe*.

the tip velocity is largely independent of *F*. The vertical tip location depends only weakly on *Pe*.

4. Gravitational instability mode

In this section, we investigate the existence of a Rayleigh–Taylor mode at the predominantly horizontal, unstably stratified interface between the two fluids. As mentioned above, there is no single reference frame in which the entire interface is quasisteady, so that we have to analyse different sections of the interface separately. This is facilitated by the nearly unidirectional flow along most of the interface, which allows us to assume a locally one-dimensional base state, as sketched in figure 7.

Rayleigh–Taylor instability between miscible fluids in Hele-Shaw cells has previously been analysed (Fernandez *et al.* 2002; Graf, Meiburg & Härtel 2002; Martin, Rakotomalala & Salin 2002; Goyal & Meiburg 2004), although in those earlier investigations the Hele-Shaw apparatus was oriented vertically. The present, horizontal configuration differs from a vertical cell in important aspects. Here, the unstable fluid layer extends infinitely in the horizontal direction, while it is bounded
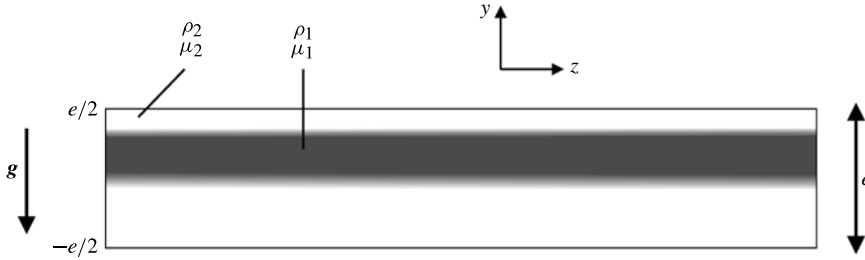
FIGURE 7. Along the unstable, predominantly horizontal interface separating the two fluids, the flow is nearly unidirectional, so that we can assume a locally one-dimensional base state that depends only on the *y*-direction.

by walls above and below. In the vertical cell, on the other hand, the fluid layer is bounded by sidewalls, while it extends infinitely in the direction of gravity. For the horizontal configuration, we expect the walls above and below to have a stabilizing effect, especially for large *F*-values, when the unstable interface is located near one of the walls. Thus, we may expect a competition between two opposing effects: on the one hand, a large gravitational parameter should amplify the Rayleigh–Taylor instability mode. On the other hand, for large *F* the interface is brought closer to the wall, which should have a stabilizing effect. A further important difference with previous work concerns the existence of a base flow velocity in the present case. A Rayleigh–Taylor instability can develop either in the streamwise ('α-mode') or the spanwise ('β-mode') direction. We expect that streamwise and spanwise perturbations will be affected differently by the base flow velocity, and it is not obvious *a priori* which mode will dominate in a given parameter regime. This issue will be clarified through the linear stability analysis to be discussed below.

4.1. *Linearization*

To perform the local linear stability analysis of the gravitational mode at the streamwise location x_0, the governing equations (2.9)–(2.11) are linearized around the *y*-dependent base state. We assume locally unidirectional flow in the *x*-direction and expand the flow variables as

$$u(x, y, z, t) = \bar{u}(x_0, y) + u'(x, y, z, t) \tag{4.1}$$

$$v(x, y, z, t) = v'(x, y, z, t) \tag{4.2}$$

$$w(x, y, z, t) = w'(x, y, z, t), \tag{4.3}$$

$$p(x, y, z, t) = \bar{p}(x_0, y) + p'(x, y, z, t), \tag{4.4}$$

$$c(x, y, z, t) = \bar{c}(x_0, y) + c'(x, y, z, t). \tag{4.5}$$

We assume then a normal mode decomposition in the streamwise (α-mode) or spanwise (β-mode) direction of the form

$$\begin{pmatrix} p' \\ w' \\ u' \\ v' \\ c' \end{pmatrix} = \begin{pmatrix} \hat{P}(y) \\ \hat{W}(y) \\ \hat{U}(y) \\ \hat{V}(y) \\ \hat{C}(y) \end{pmatrix} e^{i(\alpha x + \beta z - \omega t)}. \tag{4.6}$$

We thus obtain a generalized eigenvalue problem

$$A\boldsymbol{\phi} = -\omega B\boldsymbol{\phi}, \tag{4.7}$$

where the operators A, B and the vector $\boldsymbol{\phi}$ are defined as

$$A = \begin{pmatrix} 0 & i\beta I & i\alpha I & \partial_y & 0 \\ -i\beta I & M_1 & 0 & i\beta Re^{R(\bar{c}-1)}\dfrac{\partial\bar{c}}{\partial y}I & 0 \\ -i\alpha I & 0 & M_2 & M_3 & M_4 \\ -\partial_y & 0 & 0 & M_5 & M_6 \\ 0 & 0 & 0 & -\dfrac{\partial\bar{c}}{\partial y}I & M_7 \end{pmatrix}, \tag{4.8a}$$

$$B = \begin{pmatrix} 0 & 0 & 0 & 0 & 0 \\ 0 & iRe & 0 & 0 & 0 \\ 0 & 0 & iRe & 0 & 0 \\ 0 & 0 & 0 & iRe & 0 \\ 0 & 0 & 0 & 0 & i \end{pmatrix} \quad \text{and} \quad \boldsymbol{\phi} = \begin{pmatrix} \hat{P} \\ \hat{W} \\ \hat{U} \\ \hat{V} \\ \hat{C} \end{pmatrix}, \tag{4.8b}$$

with

$$M_1 = \left[(-\beta^2 - \alpha^2)e^{R(\bar{c}-1)} - iRe\bar{u}\alpha\right]I + Re^{R(\bar{c}-1)}\frac{\partial\bar{c}}{\partial y}\partial_y + e^{R(\bar{c}-1)}\partial_{yy}, \tag{4.9a}$$

$$M_2 = \left[(-\beta^2 - \alpha^2)e^{R(\bar{c}-1)} - iRe\bar{u}\alpha\right]I + Re^{R(\bar{c}-1)}\frac{\partial\bar{c}}{\partial y}\partial_y + e^{R(\bar{c}-1)}\partial_{yy}, \tag{4.9b}$$

$$M_3 = \left[i\alpha Re^{R(\bar{c}-1)} - Re\frac{\partial\bar{u}}{\partial y}\right]I, \tag{4.9c}$$

$$M_4 = e^{R(\bar{c}-1)}\left[\left(R^2\frac{\partial\bar{u}}{\partial y}\frac{\partial\bar{c}}{\partial y} + R\frac{\partial^2\bar{u}}{\partial y^2}\right)I + R\frac{\partial\bar{u}}{\partial y}\partial_y\right], \tag{4.9d}$$

$$M_5 = \left[(-\beta^2 - \alpha^2)e^{R(\bar{c}-1)} - iRe\bar{u}\alpha\right]I + 2Re^{R(\bar{c}-1)}\frac{\partial\bar{c}}{\partial y}\partial_y + e^{R(\bar{c}-1)}\partial_{yy}, \tag{4.9e}$$

$$M_6 = \left[i\alpha e^{R(\bar{c}-1)}\frac{\partial\bar{u}}{\partial y}R - F\right]I \tag{4.9f}$$

$$M_7 = \frac{1}{Pe}(-\alpha^2 - \beta^2)I - i\alpha\bar{u}I + \frac{1}{Pe}\partial_{yy}, \tag{4.9g}$$

where I, ∂_y and ∂_{yy} represent the identity matrix and the first and second derivative operators, respectively. Solving this eigenvalue problem leads to the growth rate σ as a function of the streamwise location x_0 and the streamwise wavenumber α or the spanwise wavenumber β. Here $\sigma^\alpha(x_0)$ and $\sigma^\beta(x_0)$ will denote the streamwise and spanwise local dispersion relations, respectively.

We note that, while the α-mode is affected by the streamwise base flow velocity profile, for $\alpha = 0$ the base velocity profile $\bar{u}(x)$ and its derivative do not enter into the stability equations, so that the β-mode reduces to the classical Rayleigh–Taylor instability. We furthermore comment that F and Pe appear as a product, which has the form of a Rayleigh number $Ra = FPe = \Delta\rho ge^3/\mu_2 D$. However, since these two
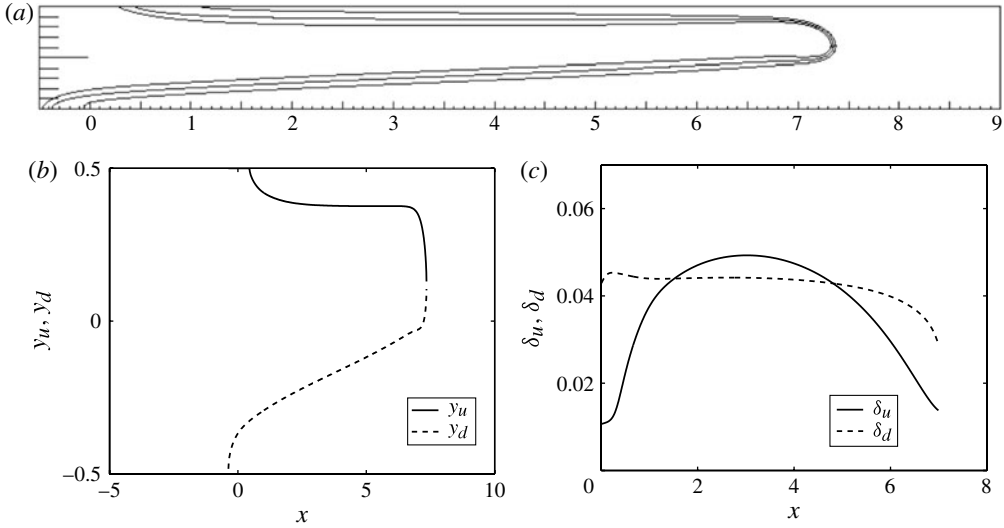
FIGURE 8. (*a*) Concentration base state from the direct numerical simulation for $F = 60$, $R = 2.5$, $Pe = 2000$ and time $t = 4.1$. (*b*) The y_u and y_d position of the $c = 0.5$ concentration contour as function of the streamwise x-location. (*c*) Interface thickness δ_u and δ_d of the upper and lower interface, respectively.

parameters individually influence the base state, they need to be considered separately. Since inertia is known to destabilize viscous shear flow, we will investigate the influence of the Reynolds number on the two instability modes (figure 18). However, unless mentioned explicitly, the results presented below will be for $Re = 0$.

In the next section, we present results of the local stability analysis. Subsequently, we perform a parametric study for different values of the two interface locations and thicknesses.

4.2. *Local stability analysis of the finger*

As a representative case, we discuss the flow for $F = 60$, $R = 2.5$ and $Pe = 2000$ at time $t = 4.1$. The base state is shown in figure 8(*a*). Figure 8(*b*) shows the *y*-locations y_u and y_d of the upper and lower interface, defined by the $c = 0.5$ concentration contour, as a function of the streamwise *x*-location. We note that in the central section $2 \leqslant x \leqslant 6.5$ of the finger, where the unidirectional flow assumption is reasonably valid, the *y*-location of the upper interface is approximately constant, while the lower interface rises in the streamwise direction.

We define the upper and lower interface thicknesses δ_u and δ_d, respectively, in terms of the root mean square (r.m.s.) of $\partial c/\partial y$

$$\delta = \sqrt{\int y^2 \frac{\partial c}{\partial y} \mathrm{d}y - \left(\int y \frac{\partial c}{\partial y} \mathrm{d}y \right)^2}. \tag{4.10}$$

This definition is particularly useful for investigating initially step-like profiles. We remark that this definition is also consistent with the parametric thickness in the error-function introduced later in (4.11), as it gives $\delta = \delta_u$ and δ_d, respectively. Figure 8(*c*) indicates that the upper interface thickness δ_u has a maximum in the central region of the finger.
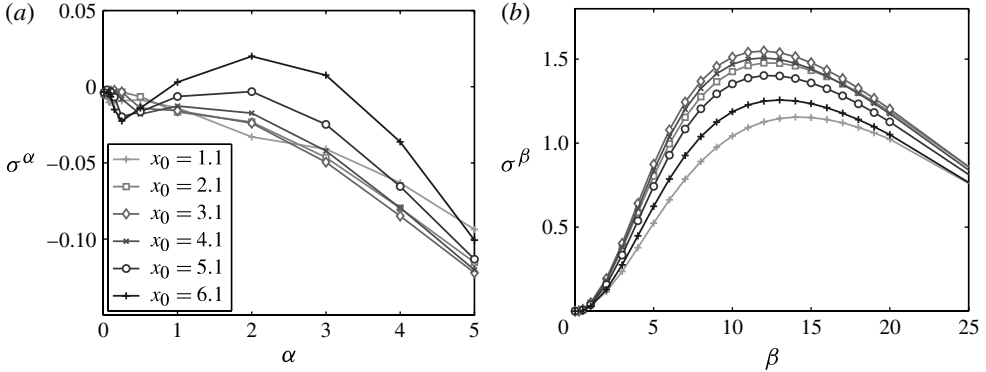
FIGURE 9. Dispersion relations $\sigma^\alpha(\alpha, x_0)$ (*a*) and $\sigma^\beta(\beta, x_0)$ (*b*) at different locations x_0 for the base state corresponding to $F = 60$, $R = 2.5$ and $Pe = 2000$ at time $t = 4.1$. Along the central section of the finger, both the maximum growth rate and the wavenumber of the most dangerous mode vary little with the streamwise location.
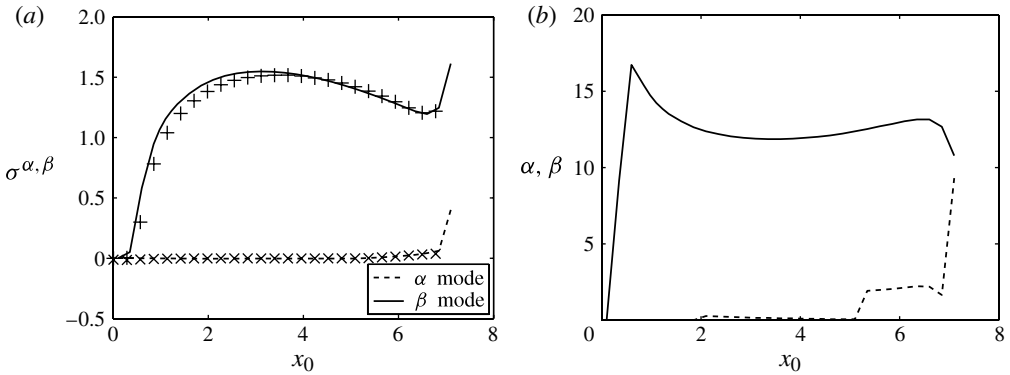
FIGURE 10. Maximum growth rate $\sigma_0^l(x_0)$ (*a*) and the corresponding, most amplified wavenumber (*b*) of the α- and β-mode as functions of x_0, for $F = 60$, $R = 2.5$ and $Pe = 2000$ at time $t = 4.1$. Along the central section of the finger, both the maximum growth rate and the wavenumber of the most dangerous mode vary little with the streamwise location. The spanwise β-mode is always more unstable than the streamwise α-mode. The symbols indicate the growth rates obtained when the parametric linear stability analysis, which will be described below, is applied for the interfacial properties shown in figure 8.

We can now perform a linear stability analysis for every location x_0, as described above. Figure 9 displays representative dispersion relations $\sigma^\alpha(\alpha, x_0)$ and $\sigma^\beta(\beta, x_0)$ for the base state depicted in figure 8.

Both the maximum growth rates $\sigma^{\alpha,\beta}(x_0)$ and the corresponding, most amplified wavenumbers show relatively little variation along the central section of the finger, as confirmed by figure 10. Note that the minima and maxima at the front and rear of the finger are unphysical, since here the unidirectional flow analysis is not valid. Clearly, at every x_0-location the spanwise instability mode exhibits a much larger growth rate than the streamwise one. In fact, the α-mode is stable along most of the interface. We note that this result is not unexpected since, if the finger were α-unstable, we should
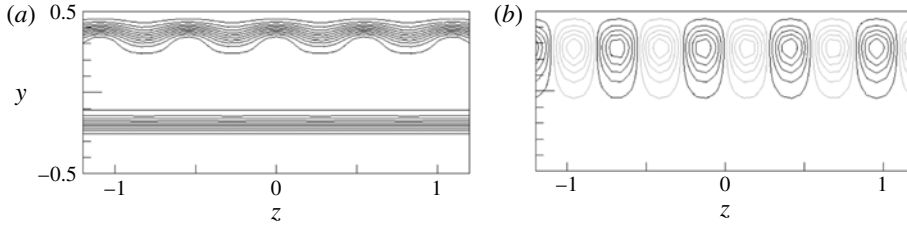
FIGURE 11. The most unstable gravitational β-mode for $F = 60$, $R = 2.5$ and $Pe = 2000$ at time $t = 4.1$. (*a*) Contours of $\hat{c}$ superimposed onto the base state. (*b*) Eigenfunction of the stream function. The instability alternately shifts the upper interface towards the top wall and away from it, while modifying its local thickness periodically in the spanwise direction.

have seen streamwise instabilities arising in the direct numerical simulation (DNS) of the two-dimensional base state. The physical interpretation of this behaviour will be discussed in the context of the parametric study.

From the results shown in figure 10, we obtain the global maximum of the growth rates σ_G^α and σ_G^β and the corresponding, most dangerous wavenumbers α_G and β_G, along with the locations x_G^α and x_G^β where they are observed. Figure 11 provides insight into the physical nature of the β-mode. It consists of a spanwise periodic array of counterrotating streamwise vortices that alternately shift the upper, unstable interface towards and away from the top wall. Those interface sections shifted closer to the wall are steepened in the process, while the downward displaced sections grow thicker. This instability mode is responsible for the 'cavity formation' observed in Part 2 (John *et al.* 2013).

The location x_G of the highest growth rate reflects the influence of two competing features, namely the vertical position and the thickness of the interface. One might expect the wall to have a stabilizing influence, which should render the rear sections of the interface more stable as compared with the forward sections, since they are located more closely to the wall. At the same time, the forward sections of the interface are thinner. Intuitively, one might associate thinner interfaces with larger growth rates. Note, however, that the maximum growth occurs near $x = 3$, where the interface is both thicker and nearer to the top wall, as compared with locations closer to the tip. This perhaps unexpected behaviour will be analysed by means of a parametric study below.

We now investigate the influence of the governing dimensionless parameters F, R and Pe on the globally most unstable mode. Figure 12 displays the dependence of the growth rate on F, for several values of the viscosity ratio. We note that for every viscosity ratio and F-value, the β-mode is far more unstable than the α-mode. The growth rate of the β-mode is seen to increase uniformly with F, in spite of the fact that the unstable interface is shifted closer to the wall. This indicates that the destabilizing effect of the increasingly unstable density stratification outweighs the stabilizing effect of the top wall. Stronger viscosity contrasts are found to enhance the growth rate. Since we employed the larger viscosity when rendering the governing equations dimensionless, this means that for a constant viscosity resident fluid, lowering the viscosity of the injected fluid results in a more vigorous instability. Note that this observation is not in contrast to the findings of Goyal & Meiburg (2004) for the Rayleigh–Taylor instability in a vertical Hele-Shaw cell. Those authors found that an increase in the viscosity ratio had a stabilizing effect. However, they
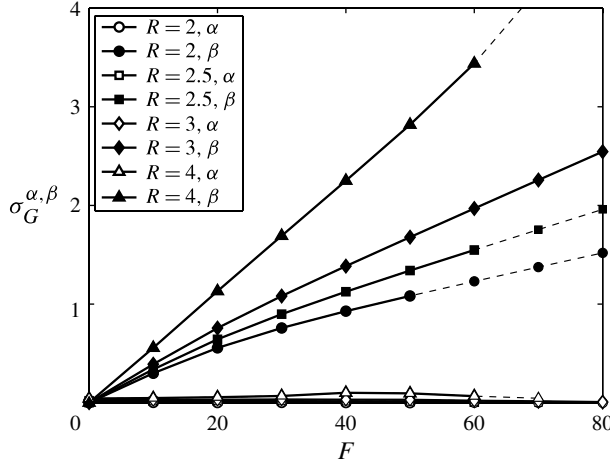
FIGURE 12. Growth rates of the globally most unstable α- and β-modes, as functions of the gravity parameter F for different viscosity ratios and $Pe = 2000$.
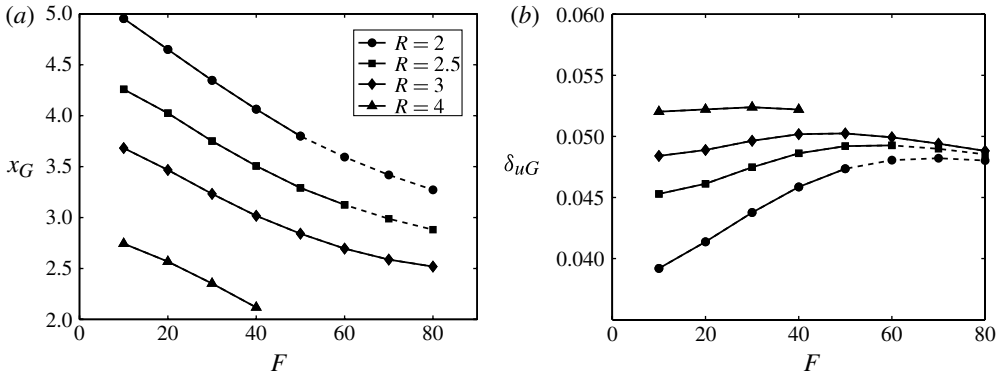
FIGURE 13. Location x_G of the globally most unstable β-mode, along with the thickness of the upper interface at this location. $Pe = 2000$ for all cases.

had employed the lower viscosity for the purpose of non-dimensionalizing. Hence, an increase in the viscosity ratio corresponds to using increasingly viscous resident fluids, which should be stabilizing. In Goyal *et al.* (2007) the authors normalize with the larger viscosity and, similarly to our current findings, they observe an increase in the viscosity contrast to be destabilizing.

Figure 13 displays several characteristics of the base state at the streamwise location x_G of the globally most unstable β-mode. For increasing F-values the instability location moves towards the rear of the finger, and thus closer to the top wall, into a region where the effective interface thickness δ_{uG} is somewhat larger. The reasons for this observation will become clear from the parametric study to be discussed below.

The dependence of $\sigma_G^{\alpha,\beta}$ on the Péclet number is shown in figure 14. Consistent with previous work for vertical Hele-Shaw cells, variations in Pe affect the instability only
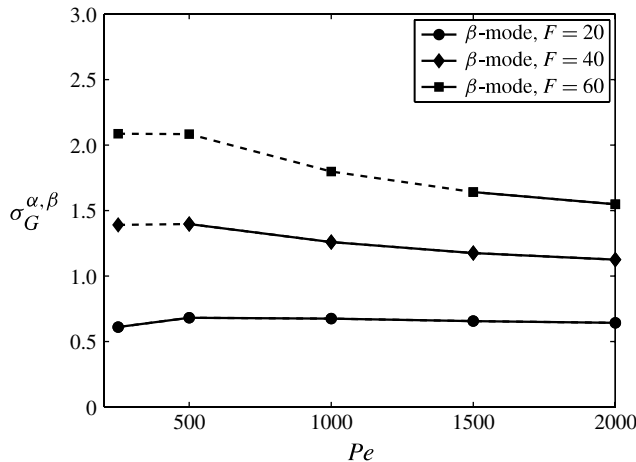
FIGURE 14. The global maximum of the growth rate $\sigma_G^{\alpha,\beta}$, as function of the Péclet number for different values of F and $R = 2.5$.

mildly. As Pe increases, the instability is enhanced somewhat for small F, while its growth is reduced for higher F.

4.3. *Parametric stability analysis*

In order to investigate independently the influence of the interface thickness and the proximity of the wall on the instability, we perform a parametric stability analysis for a prototype interface. Towards this end, we define the concentration base profile as

$$\bar{c}(y) = \frac{1}{2} - \frac{1}{2}\mathrm{erf}\left(\frac{y - y_d}{\sqrt{2}\delta_d}\right) + \frac{1}{2} + \frac{1}{2}\mathrm{erf}\left(\frac{y - y_u}{\sqrt{2}\delta_u}\right). \tag{4.11}$$

The unidirectional velocity profile $\bar{u}(y)$ is deduced by a double integration of the one-dimensional momentum balance for a given viscosity profile, subject to the constraint that the average streamwise velocity has to be unity. The growth rates of the α- and β-modes then become functions of both R, F and Pe, and of the two interface positions (y_u, y_d) and thicknesses (δ_u, δ_d). Note that we also incorporate the possibility to have a non-zero Reynolds number Re, in order to check the validity of the Stokes flow assumption.

Figure 15 shows the growth rates σ_P^α and σ_P^β as functions of the two interface positions (y_u, y_d) for $Re = 0$, $R = 2.5$, $F = 60$, $Pe = 2000$ and $\delta_u = \delta_d = 0.01$. We note that the maximum growth rate for both modes occurs for $y_d = -0.5$, i.e. when the lower interface coincides with the bottom wall, so that effectively there is only the upper, gravitationally unstable interface. In this case, the instabilities are most pronounced when the upper, denser and more viscous fluid layer is somewhat thicker than the lower one. On the other hand, if the upper interface is located close to the upper wall or to the lower interface, the growth of the instability is damped. For $y_u \gtrsim 0.2$, the growth rate is nearly independent of the lower interface position, as long as the two interfaces are sufficiently far apart.

Interestingly, figure 15 indicates that the maximum growth rates of the α- and β-modes are similar in magnitude. At first glance this may be unexpected, since figure 12 had shown that for the DNS base state the spanwise β-mode grows much
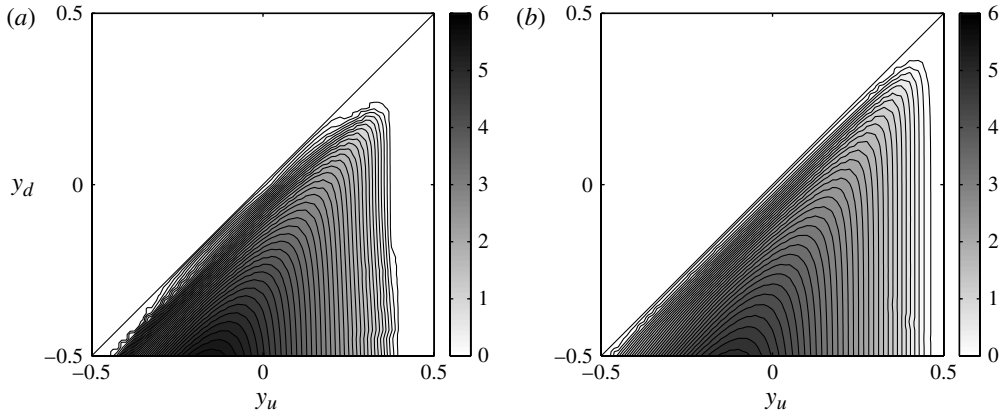
FIGURE 15. Parametric growth rates σ_P^α of the streamwise mode (*a*) and σ_P^β of the spanwise mode (*b*), as functions of the upper y_u and lower y_d interface locations. The other parameter values are $Re = 0$, $R = 2.5$, $F = 60$, $Pe = 2000$ and $\delta_u = \delta_d = 0.01$.

faster than the streamwise α-mode. Here it is important to keep in mind that the DNS base state is characterized by an upper interface location of $y_u \approx 0.4$, for which figure 15 indeed shows that spanwise waves grow much faster than their streamwise counterparts.

In order to assess which mode dominates in which parameter regime, figure 16 displays the difference of the growth rates $\sigma_P^\beta - \sigma_P^\alpha$ as a function of the interface locations. We note that for $y_u \gtrsim 0.1$ the spanwise β-mode generally dominates, whereas for $y_u \lesssim 0.1$ there exists a large region dominated by the streamwise α-mode. We conclude that the proximity of the upper wall to the interface dampens the streamwise mode more strongly than the spanwise one.

The thick black line and the open white circles in figure 16 indicate all of the interface locations corresponding to the DNS. While the thick black line represents those interface segments along which the streamwise derivative $dy_u(x)/dx < 0.01$, the white circles denote the segments with stronger slopes, where the parallel flow assumption may be less well satisfied. We recognize that the entire interface lies in the region where the spanwise mode dominates. In fact, it approximately follows a path where the dominance of the β-mode is most pronounced.

In summary, figure 16 suggests that the dominance of the β-mode over the α-mode observed in the stability analysis of §4.2 is a consequence of the gravitational shift of the upper interface toward the upper wall, and the stronger damping of the α-mode by the resulting proximity of the wall. Figure 17 presents corresponding results for $F = 20$ and 40, which display a similar trend.

We now briefly analyse the influence of Re, Pe and the thickness of the gravitationally unstable interface for a representative pair of interface locations $(y_u; y_d) = (0.4; -0.2)$. It is well known that inertia can destabilize sheared viscous flow (e.g. Yih 1967; Hinch 1984; Selvam *et al.* 2009) with a growth rate proportional to the Reynolds number. Our objective here is to see how inertia might affect the gravitational modes. Figure 18 shows that for $Re \leqslant 40$ the influence of the Reynolds number on the growth rates of the two modes is very small, which justifies the Stokes flow assumption made earlier. The influence of the thickness of the upper interface is somewhat counterintuitive. Figure 19 indicates that the growth rate of
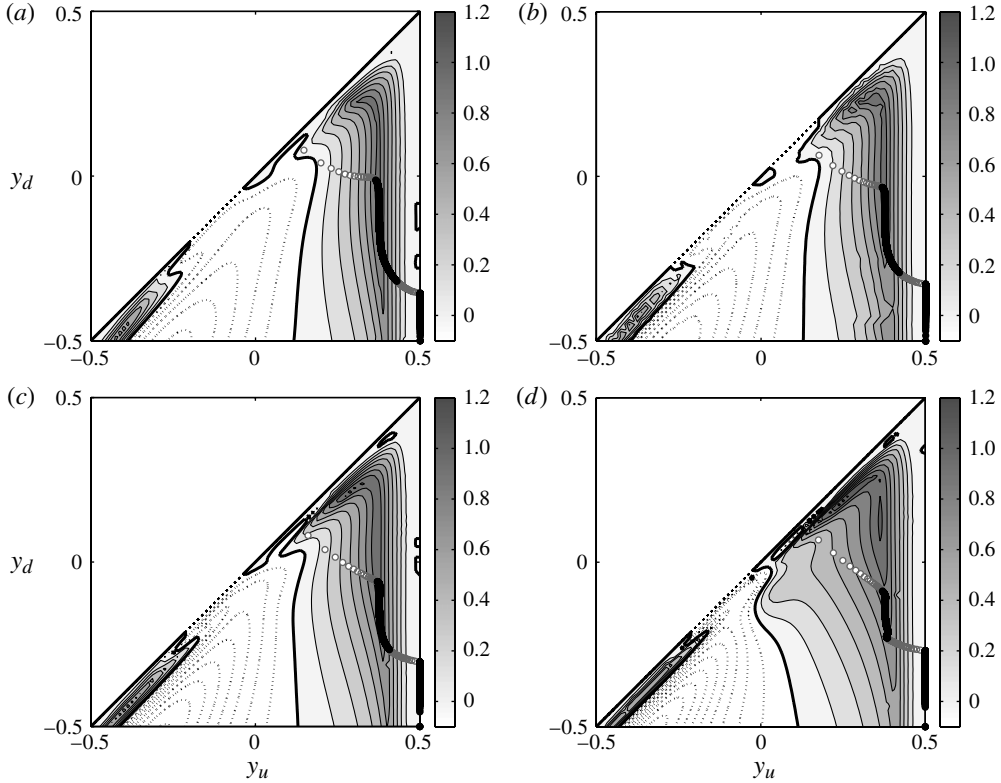
FIGURE 16. Difference of the growth rates $\sigma_P^\beta - \sigma_P^\alpha$ as a function of the upper y_u and lower y_d interface locations, for different values of the viscosity parameter R. The other parameter values are $Re = 0$, $F = 60$, $Pe = 2000$ and $\delta_u = \delta_d = 0.01$. The contour $\sigma_P^\beta - \sigma_P^\alpha = 0$ is highlighted by a somewhat thicker line. The open white circles and very thick black line represent the interface locations $(y_u(x), y_d(x))$ corresponding to the DNS, e.g. figure 8: (a) $R = 2, \sigma_P^\beta - \sigma_P^\alpha$; (b) $R = 2.5, \sigma_P^\beta - \sigma_P^\alpha$; (c) $R = 3, \sigma_P^\beta - \sigma_P^\alpha$; (d) $R = 4, \sigma_P^\beta - \sigma_P^\alpha$.

the β-mode increases with the interface thickness. This observation resembles our earlier findings for Rayleigh–Taylor instabilities in vertical Hele-Shaw cells (Goyal & Meiburg 2004), which also showed that for variable viscosity fluids, thicker interfaces can be more unstable than thinner ones. A similar behaviour was also observed for shear instabilities between fluids of different viscosities (Talon & Meiburg 2011). We remark that for very thick interfaces the growth rate would decrease again (not shown in the figure), as the driving density gradient decreases, so that the most rapid growth occurs for an intermediate thickness δ_u. This explains the unexpected result found in § 4.2 that the maximum growth rate occurs where the upper interface is thickest.

Not surprisingly, as discussed above, for a constant F-value the growth rate of the β-mode increases with the Péclet number, i.e. with the Rayleigh number (FPe). We note moreover that the growth rate seems to saturate for large Pe numbers, consistent with the observations in Goyal & Meiburg (2004). Interestingly, the growth rate of the α-mode increases rapidly above $Pe \approx 2000$. As discussed above, the streamwise α-mode is also affected by the unstable density stratification. For the current combination of interfaces positions, the streamwise shear flow has a stabilizing effect, but for large
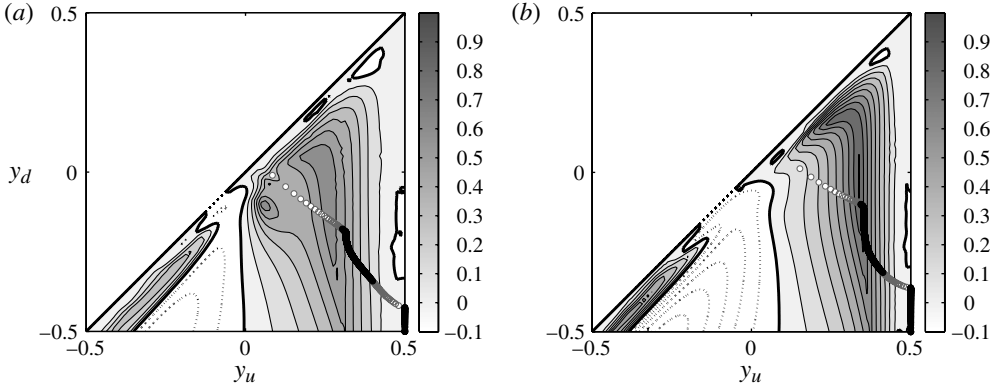
FIGURE 17. Difference of the parametric growth rate $\sigma_P^\beta - \sigma_P^\alpha$ (b) as a function of the upper y_u and lower y_d interface positions, for different values of the gravitational parameter F. The other parameters are $Re = 0$, $R = 2.5$, $Pe = 2000$ and $\delta_u = \delta_d = 0.01$. The circle symbols represent the interface position $(y_u(x), y_d(x))$ found from DNSs. Open white symbols represent the position where the derivative exceeds 1 %: (a) $R = 2.5$, $F = 20$, $\sigma_P^\beta - \sigma_P^\alpha$; (b) $R = 2.5$, $F = 40$, $\sigma_P^\beta - \sigma_P^\alpha$.
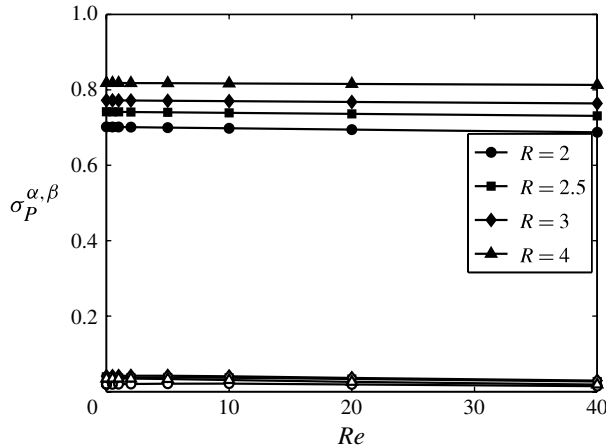
FIGURE 18. Parametric growth rates σ_P^β (filled symbol) and σ_P^α (open symbol) as functions of the Reynolds number Re for the interface locations $y_u = 0.4$ and $y_d = -0.2$. The other parameter values are $R = 2.5$, $F = 60$, $Pe = 2000$ and $\delta_u = \delta_d = 0.01$.

Péclet (and thus the Rayleigh) numbers, the gravitational instability tends to overcome this stabilizing effect of the shear flow.

5. Viscous mode

For the purpose of investigating the tip instability mode, we follow the approach employed by Goyal & Meiburg (2006) for the neutrally buoyant case. By analysing the quasisteady base flow in a moving reference frame, we obtain a computational eigenvalue problem in a two-dimensional domain around the tip of the form of (4.7)
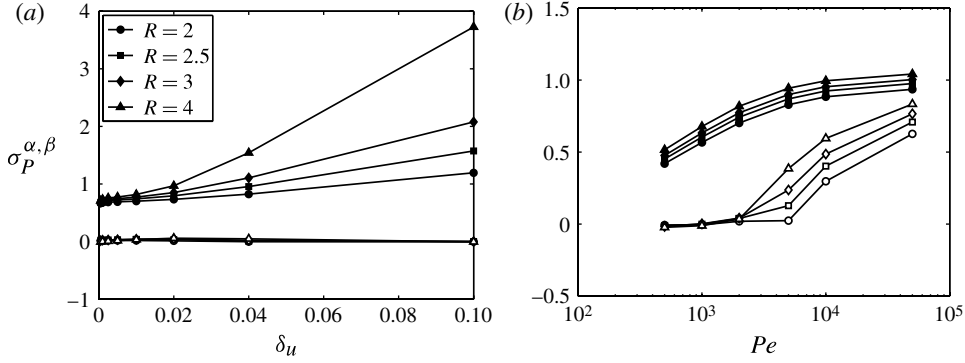
FIGURE 19. Parametric growth rate σ_P^β (filled symbols) and σ_P^α (open symbols) as functions of the upper interface thickness (*a*) and the Péclet number (*b*), for the interface locations $y_u = 0.4$ and $y_d = -0.2$. The values of the other parameters are $R = 2.5$, $F = 60$, $Pe = 2000$ and $\delta_u = \delta_d = 0.01$.

with

$$
A = \begin{pmatrix}
0 & \beta I & \partial_x & \partial_y & 0 \\
\beta I & M_1 & -\beta e^{R(\bar{c}-1)} R \dfrac{\partial \bar{c}}{\partial x} I & -\beta e^{R(\bar{c}-1)} R \dfrac{\partial \bar{c}}{\partial y} I & 0 \\
-\partial_x & 0 & M_2 & Re^{R(\bar{c}-1)} \dfrac{\partial \bar{c}}{\partial y} \partial_x & M_3 \\
-\partial_y & 0 & Re^{R(\bar{c}-1)} \dfrac{\partial \bar{c}}{\partial x} \partial_y & M_4 & M_5 \\
0 & 0 & -\dfrac{\partial \bar{c}}{\partial x} I & -\dfrac{\partial \bar{c}}{\partial y} I & M_6
\end{pmatrix}, \tag{5.1}
$$

where

$$
M_1 = e^{R(\bar{c}-1)} \left(R \frac{\partial \bar{c}}{\partial x} \partial_x + R \frac{\partial \bar{c}}{\partial y} \partial_y + \partial_{yy} + \partial_{xx} - \beta^2 I \right), \tag{5.2a}
$$

$$
M_2 = e^{R(\bar{c}-1)} \left(2R \frac{\partial \bar{c}}{\partial x} \partial_x + R \frac{\partial \bar{c}}{\partial y} \partial_y + \partial_{yy} + \partial_{xx} - \beta^2 I \right), \tag{5.2b}
$$

$$
M_3 = Re^{R(\bar{c}-1)} \left(\left(2R \frac{\partial \bar{c}}{\partial x} \frac{\partial \bar{u}}{\partial x} + R \frac{\partial \bar{c}}{\partial y} \left(\frac{\partial \bar{u}}{\partial y} + \frac{\partial \bar{v}}{\partial y} \right) + \frac{\partial^2 \bar{u}}{\partial y^2} + \frac{\partial^2 \bar{u}}{\partial x^2} \right) I \right.
$$
$$
\left. + \left(\frac{\partial \bar{u}}{\partial y} + \frac{\partial \bar{v}}{\partial y} \right) \partial_y + 2 \frac{\partial \bar{u}}{\partial x} \partial_x \right), \tag{5.2c}
$$

$$
M_4 = e^{R(\bar{c}-1)} \left(-\beta^2 I + R \frac{\partial \bar{c}}{\partial x} \partial_x + 2R \frac{\partial \bar{c}}{\partial y} \partial_y + \partial_{yy} + \partial_{xx} \right), \tag{5.2d}
$$

$$
M_5 = \left(R^2 e^{R(\bar{c}-1)} \frac{\partial \bar{c}}{\partial x} \left(\frac{\partial \bar{u}}{\partial y} + \frac{\partial \bar{v}}{\partial y} \right) + 2R^2 e^{R(\bar{c}-1)} \frac{\partial \bar{v}}{\partial y} \frac{\partial \bar{c}}{\partial y} \right.
$$
$$
\left. + Re^{R(\bar{c}-1)} \left(\frac{\partial^2 \bar{v}}{\partial y^2} + \frac{\partial^2 \bar{v}}{\partial x^2} \right) - F \right) I
$$
$$
+ Re^{R(\bar{c}-1)} \left(\frac{\partial \bar{u}}{\partial y} + \frac{\partial \bar{v}}{\partial y} \right) \partial_x + 2Re^{R(\bar{c}-1)} \frac{\partial \bar{v}}{\partial y} \partial_y, \tag{5.2e}
$$

$x_{tip} - x_{cut}$	1st mode σ	2nd mode σ
5.5	0.697995	0.228195
4.5	0.697995	0.161296
3.5	0.697995	0.098228
2.5	0.697995	0.042463
1.5	0.697932	−0.00023

TABLE 1. Growth rate of the first and second instability modes for different values of x_{cut}, for $R = 2.5$, $F = 60$, $Pe = 2000$ and $\beta = 4.5$. Although the growth rate of the second, gravitational mode depends on x_{cut}, the dominant, viscous mode is not affected.

$$M_6 = \frac{1}{Pe}(-\beta^2 I + \partial_{yy} + \partial_{xx}) - \bar{u}\partial_x - \bar{v}\partial_y, \qquad (5.2f)$$

$$B = \begin{pmatrix} 0 & 0 & 0 & 0 & 0 \\ 0 & 0 & 0 & 0 & 0 \\ 0 & 0 & 0 & 0 & 0 \\ 0 & 0 & 0 & 0 & 0 \\ 0 & 0 & 0 & 0 & I \end{pmatrix} \quad \text{and} \quad \boldsymbol{\phi} = \begin{pmatrix} \hat{P} \\ \hat{W} \\ \hat{U} \\ \hat{V} \\ \hat{C} \end{pmatrix}. \qquad (5.3)$$

Its solution yields the shape of the dominant mode along with the corresponding growth rate. Since the use of a moving reference frame is appropriate for the region near the tip only, we employ a computational domain that extends a few gap widths on either side of the tip. At the domain boundaries we need to satisfy Neumann boundary conditions for the eigenfunctions. Towards this end, we suppress the gravitational instability mode along the upper, unstable interface at those domain boundaries far ahead and behind the tip. This can be accomplished by artificially reducing the gravity parameter F to zero a certain distance behind the tip, in a gradual fashion. To be precise, we introduce an artificial x-dependence of F in the form

$$F(x) = F\left(\tfrac{1}{2} + \tfrac{1}{2}\mathrm{erf}(2(x - x_{cut}))\right), \qquad (5.4)$$

where x_{cut} defines a position sufficiently far behind the tip location. Typically, in our computations $x_{tip} - x_{cut} \sim 5$, which is sufficient for the properties of the tip instability mode not to be affected (see table 1).

Figure 20 compares the eigenfunctions of the neutrally buoyant case ($F = 0$, figure 20a) with the variable density case ($F = 60$, figure 20b) for $R = 2.5$, $Pe = 2000$ and $\beta = 4.5$. As the gravity parameter increases, the centre of the tip instability mode shifts towards the upper interface, where it is reinforced by the unstable density stratification. At $F = 60$, both the perturbation concentration and the associated velocities are essentially limited to the upper half of the gap. In this way, the roll-like structure of the perturbation velocity field observed by Goyal & Meiburg (2006) for the neutrally buoyant case becomes distorted, as the dominant axis of rotation acquires a streamwise component in addition to the cross-gap component. Figure 21 provides quantitative information on the influence of density variations in the presence of a gravitational field. The dispersion relations $\sigma^v(k)$ for $R = 2.5$, $Pe = 2000$ show that as F increases, the most unstable mode is shifted towards shorter wavelengths. At the same time, the maximum growth rate is enhanced.
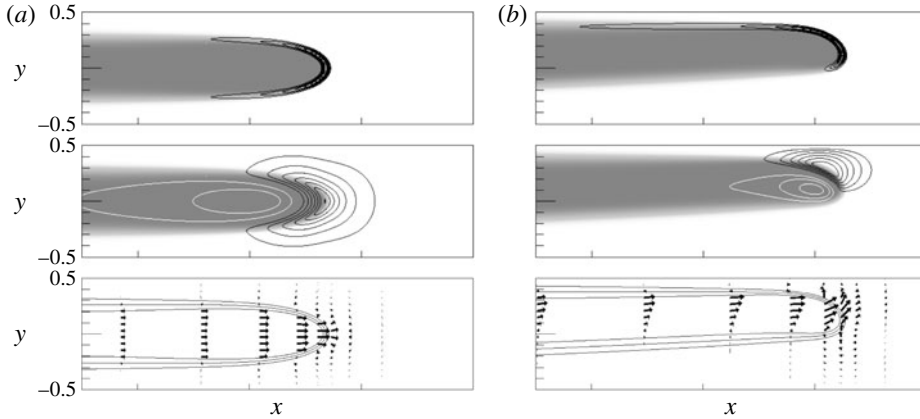
FIGURE 20. Eigenfunctions (from top to bottom) $\hat{c}$, $\hat{w}$ and the vector field $(\hat{u}, \hat{v})$ superimposed onto the concentration base state for $R = 2.5$, $Pe = 2000$ and $\beta = 4.5$. (*a*) The neutrally buoyant case $F = 0$. (*b*) The variable density case $F = 60$. In the presence of a density difference, the centre of the tip instability mode shifts towards the unstably stratified interface.
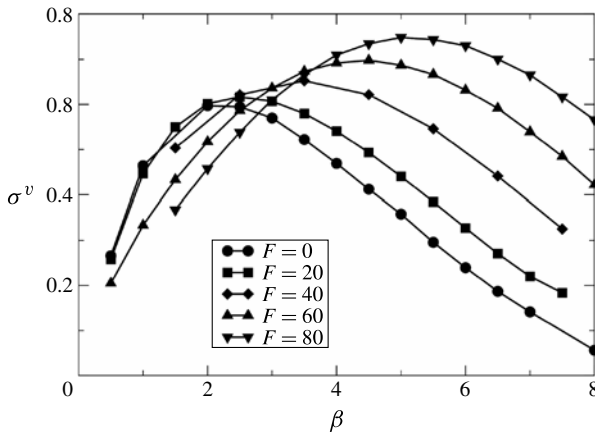
FIGURE 21. Dispersion relations $\sigma^v(k)$ for $R = 2.5$, $Pe = 2000$ and various values of F. An increase in F results in higher growth rates, while shifting the most dangerous mode towards shorter wavelengths.

Figure 22 displays both the growth rate σ_M^v and the wavenumber β_M^v of the most unstable tip instability mode as functions of F, for various R-values and $Pe = 2000$. An increase in the density contrast generally results in a mild amplification of the growth. This effect is more pronounced for larger viscosity contrasts. In light of the significant differences between the base states for small and large F (cf. figure 20), the relatively small influence of F on the growth rate is perhaps surprising. Similarly to the pure viscous fingering instability, larger viscosity contrasts have a destabilizing effect at all values of F. Larger density contrasts uniformly reduce the wavelength of the most unstable mode for all viscosity ratios. This effect is more pronounced for small values of R.
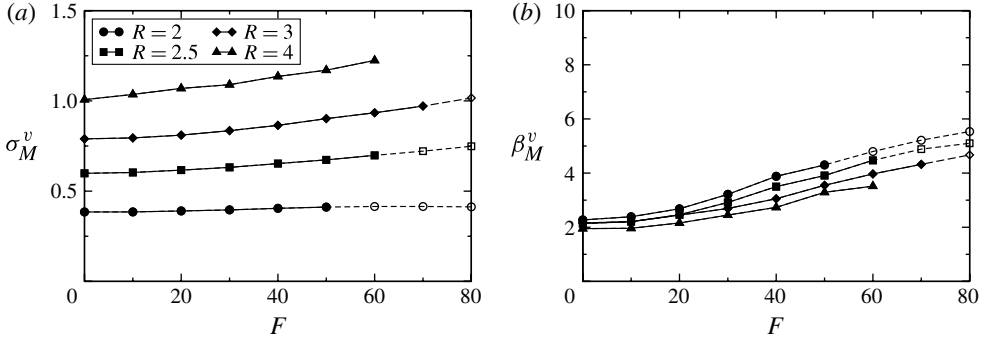
FIGURE 22. Growth rate (*a*) and wavenumber (*b*) of the most unstable tip mode as function of F, for different viscosity ratios and $Pe = 2000$.
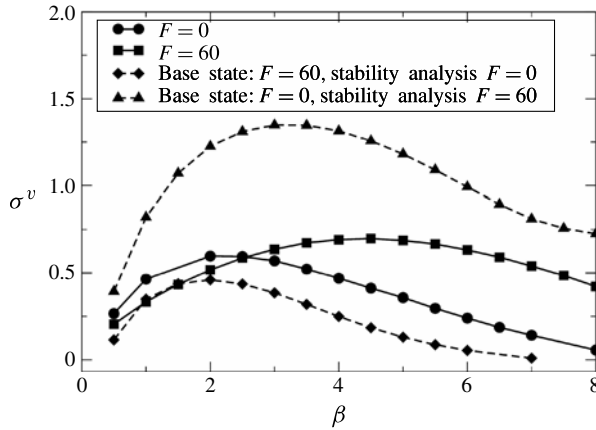
FIGURE 23. Dispersion relation $\sigma^v(k)$ for $R = 2.5$, $Pe = 2000$, $F = 0$ (circle) and $F = 60$ (square). The dashed line with diamonds corresponds to a base state obtained for $F = 60$, but with the gravity term having been removed from the stability analysis. The dashed line with triangles corresponds to a base state obtained for $F = 0$, but $F = 60$ in the stability analysis.

Gravity affects the present stability problem in two fundamentally different ways. First of all, it modifies the base state by breaking the symmetry of the displacement front with respect to the centre plane of the Hele-Shaw cell, as discussed above in § 3. Second, the presence of density variations in a gravitational field results in additional terms in the linearized stability equations. In order to establish which of these two effects dominates, we carried out two additional calculations. In the first, we employed the base state for $F = 0$, $R = 2.5$ and $Pe = 2000$, but retain the gravitational terms for $F = 60$ in the stability calculation. In the second, we employed the base state for $F = 60$, $R = 2.5$ and $Pe = 2000$, but eliminated the gravitational terms from the stability calculation. Figure 23 displays the corresponding dispersion relations. They show that the change in the base state as a result of gravity is stabilizing, while the presence of gravitational effects in the stability equations increases the growth rate and shifts the most amplified mode to shorter wavelengths. We conclude that the growth of the tip instability is governed by the competition of two effects. The symmetry of

the base state is broken for $F \neq 0$ and the finger moves towards the wall, which is stabilizing. On the other hand, the presence of the unstable density stratification in a gravitational field is destabilizing. This effect dominates, so that overall the growth rate of the tip instability mode increases with F.

6. Discussion and conclusions

We have analysed the linear stability of variable density and viscosity, miscible displacements in a Hele-Shaw apparatus. In contrast to previous investigations (Wooding 1969; Goyal *et al.* 2007), the current study has been focused on horizontal Hele-Shaw cells, in which the influence of gravity on the base state and its linear stability is quite distinct from vertical cells. As a first step, we obtained the two-dimensional base states by means of nonlinear Stokes simulations. We found that, even though gravity is oriented perpendicularly to the displacement direction, the vertical position of the displacement front reaches an quasisteady equilibrium value. This reflects a balance between viscous and gravitational forces that prevents the displacement front from reaching the horizontal wall. The quasisteady tip propagation velocity, and the length of the transient phase required to reach this velocity, both increase with the gravity parameter.

The above family of base states allows for two different instability modes. First, there is the familiar tip instability, which is driven by the unfavourable viscosity contrast of the displacement, and which may be modulated by the presence of density variations in a gravitational field. Second, we may expect a primarily gravitational instability to occur along the unstably stratified horizontal interface of the base state finger. In order to investigate these instabilities in detail, it is important to realize that the base state is characterized by three main regions that need to be treated differently. The tip of the displacement front is quasisteady in a reference frame moving with the tip propagation velocity, and hence its linear stability needs to be studied in this reference frame. The root of the finger is nearly quasisteady in the laboratory reference frame. However, a close inspection of this region does not reveal any instability. Finally, the section connecting the tip of the finger to its root is characterized by a nearly unidirectional flow, so that its linear stability can be evaluated by analysing a series of one-dimensional base states.

For the gravitational mode along the upper side of the finger, the investigation shows that it becomes more unstable as the gravity parameter increases. This result is not obvious since for higher gravity numbers the interface is located closer to the wall, which can be expected to have a stabilizing effect. Interestingly, the gravitational instability sees the highest growth rates far behind the finger tip, where the interface is both thicker and located closer to the wall than near the finger tip. The competing influences of interface thickness and wall proximity are clarified by means of a parametric stability analysis. Moreover, it is shown that the proximity of the upper wall to the interface suppresses the streamwise instability modes. Overall, the gravitational mode is characterized by a wavelength of about one half the gap width, which is about three to five times shorter than for the dominant tip instability mode.

The tip instability mode represents a gravity-modulated version of the neutrally buoyant mode identified by Goyal & Meiburg (2004). The analysis shows that in the presence of density stratification the growth rate increases slightly, while the dominant wavelength decreases. This overall destabilizing effect of gravity is due to the additional terms appearing in the linearized stability problem, which outweigh the stabilizing effects of gravity onto the base state.
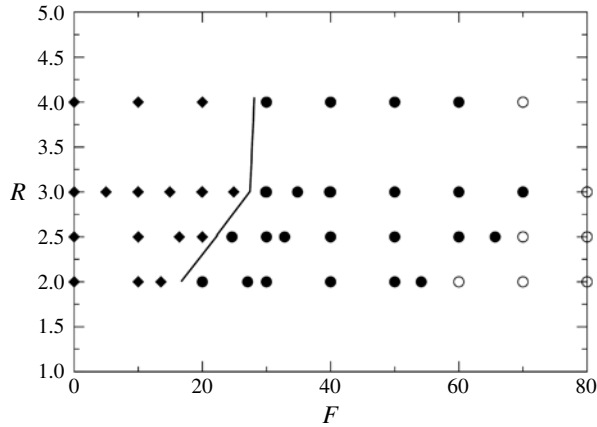
FIGURE 24. Comparison of the gravitational and tip modes in the (F, R)-plane. Diamonds: the viscous tip mode has a larger growth rate. Circles: the gravitational mode has a larger growth rate. Open symbols correspond to parameter combinations for which a fully quasisteady state was not reached.

It is of interest to determine where in the (F, R)-plane which of the two above instability modes dominates. Towards this end, figure 24 distinguishes regions according to which mode has the larger growth rate. The viscous mode is seen to dominate for small F, whereas for larger F the gravitational mode has the higher growth rate. However, it is to be kept in mind that these two instability modes appear in different parts of the flow field, so that throughout most of the (R, F)-plane we expect them to coexist, with the gravitational mode characterized by a smaller wavelength as compared to the viscous tip mode. In Part 2 of this investigation (John *et al.* 2013), we will conduct high-resolution, three-dimensional numerical simulations, in order to obtain insight into the nonlinear evolution of the viscous and gravitational instabilities.

Acknowledgements

REFERENCES

AUBERTIN, A., GAUTHIER, G., MARTIN, J., SALIN, D. & TALON, L. 2009 Miscible viscous fingering in microgravity. *Phys. Fluids* **21**, 054107.

BACRI, J.-C, RAKOTOMALALA, N. & SALIN, D. 1991 Three-dimensional miscible viscous fingering in porous media. *Phys. Rev. Lett.* **67**, 2005.

CHEN, C.-Y. & MEIBURG, E. 1996 Miscible Displacement in capillary tubes. Part 2. Numerical simulations. *J. Fluid Mech.* **326**, 57–67.

D'OLCE, M., MARTIN, J., RAKOTOMALALA, N., SALIN, D. & TALON, L. 2008 Pearl and mushroom instability patterns in two miscible fluids core annular flow. *Phys. Fluids* **20**, 24104.

D'OLCE, M., MARTIN, J., RAKOTOMALALA, N., SALIN, D. & TALON, L. 2009 Convective/absolute instability in miscible core-annular flow. Part 1: Experiments. *J. Fluid Mech.* **618**, 305–311.

FERNANDEZ, J., KUROWSKI, P., PETITJEANS, P. & MEIBURG, E. 2002 Density-driven unstable flows of miscible fluids in a Hele-Shaw cell. *J. Fluid Mech.* **451**, 239–260.

GOVINDARAJAN, R. 2004 Effect of miscibility on the linear instability of two-fluid channel flow. *Intl J. Multiphase Flow* **30**, 1177.

GOYAL, N. & MEIBURG, E. 2004 Unstable density stratification of miscible fluids in a vertical Hele-Shaw cell: influence of variable viscosity on the linear stability. *J. Fluid Mech.* **516**, 211–238.

GOYAL, N. & MEIBURG, E. 2006 Miscible displacements in Hele-Shaw cells: two-dimensional base states and their linear stability. *J. Fluid Mech.* **558**, 329–355.

GOYAL, N., PICHLER, H. & MEIBURG, E. 2007 Variable-density miscible displacements in a vertical Hele-Shaw cell: linear stability. *J. Fluid Mech.* **584**, 357–372.

GRAF, F., MEIBURG, E. & HÄRTEL, C. 2002 Density-driven instabilities of miscible fluids in a Hele-Shaw cell: linear stability analysis of the three-dimensional Stokes equations. *J. Fluid Mech.* **451**, 261–282.

HÄRTEL, C., MEIBURG, E. & NECKER, F. 2000 Analysis and direct numerical simulation of the flow at a gravity current head. Part 1: flow topology and front speed for slip and boundaries. *J. Fluid Mech.* **418**, 189–212.

HINCH, E. J. 1984 A note on the mechanism of the instability at the interface between two shearing fluids. *J. Fluid Mech.* **144**, 463–465.

HOMSY, G. M. 1987 Viscous fingering in porous media. *Annu. Rev. Fluid Mech.* **19**.

JOHN, M. O., OLIVEIRA, R. M., HEUSSLER, F. H. C. & MEIBURG, E. 2013 Variable density and viscosity, miscible displacements in horizontal Hele-Shaw cells. Part 2. Nonlinear simulations. *J. Fluid Mech.* **721**, 295–323.

LAJEUNESSE, E., MARTIN, J., RAKOTOMALALA, N. & SALIN, D. 1997 3D instability of miscible displacements in a Hele-Shaw cell. *Phys. Rev. Lett.* **79**, 5254–5257.

LAJEUNESSE, E., MARTIN, J., RAKOTOMALALA, N., SALIN, D. & YORTSOS, Y. C. 1999 Miscible displacement in a Hell–Shaw cell at high rates. *J. Fluid Mech.* **398**, 299–319.

MANICKAM, F. J. & HOMSY, G. M. 1993 Stability of miscible displacements in porous media with non-monotonic viscosity profiles. *Phys. Fluids* **A.5**, 1356–1367.

MARTIN, J., RAKOTOMALALA, N. & SALIN, D. 2002 Gravitational instability of miscible fluids in a Hele-Shaw cell. *Phys. Fluids* **14**, 902–905.

MARTIN, J., RAKOTOMALALA, N., TALON, L. & SALIN, D. 2011 Viscous lock-exchange in different geometries. *J. Fluid Mech.* **673**, 132–146.

OLIVEIRA, R. M. & MEIBURG, E. 2011 Miscible displacements in Hele-Shaw cells: three-dimensional Navier–Stokes simulations. *J. Fluid Mech.* **687**, 431–460.

PETITJEANS, P. & MAXWORTHY, T. 1996 Miscible displacements in capillary tubes. Part 1. Experiments. *J. Fluid Mech.* **326**, 37–56.

RAKOTOMALALA, N., SALIN, D. & WATZKY, P. 1997*a* Fingering in 2D parallel viscous flow. *J. Phys. II France* **7**, 967–972.

RAKOTOMALALA, N., SALIN, D. & WATZKY, P. 1997*b* Miscible displacement between two parallel plates: BGK lattice gas simulations. *J. Fluid Mech.* **338**, 277–297.

SAHU, K. C., DING, H., VALLURI, P. & MATAR, O. K. 2009*a* Linear stability analysis and numerical simulation of miscible two-layer channel flow. *Phys. Fluids* **21**, 042104.

SAHU, K. C., DING, H., VALLURI, P. & MATAR, O. K. 2009*b* Pressure-driven miscible two-fluid channel flow with density gradients. *Phys. Fluids* **21** (4).

SELVAM, B., MERK, S., GOVINDARAJAN, R. & MEIBURG, E. 2007 Stability of miscible core-annular flow with viscosity stratification. *J. Fluid Mech.* **592**, 23–49.

SELVAM, B., TALON, L., LESSHAFT, L. & MEIBURG, E. 2009 Convective/absolute instability in miscible core-annular flow. Part 2: numerical simulation and nonlinear global modes. *J. Fluid Mech.* **618**, 323–348.

SÉON, T., HULIN, J. P., SALIN, D., PERRIN, B. & HINCH, E. J. 2004 Buoyant mixing of miscible fluids in tilted tube. *Phys. Fluids* **16**, 103.

SÉON, T., HULIN, J. P., SALIN, D., PERRIN, B. & HINCH, E. J. 2005 Buoyancy driven miscible front dynamics in tilted tubes. *Phys. Fluids* **17** (3).

SÉON, T., HULIN, J. P., SALIN, D., PERRIN, B. & HINCH, E. J. 2006 Laser-induced fluorescence measurements of buoyancy driven mixing in tilted tubes. *Phys. Fluids* **18** (4).

SÉON, T., ZNAIEN, J., PERRIN, B., HINCH, E. J., SALIN, D. & HULIN, J. P. 2007*a* Front dynamics and macroscopic diffusion in buoyant mixing in a tilted tube. *Phys. Fluids* **19** (12).

SÉON, T., ZNAIEN, J., SALIN, D., HULIN, J. P., HINCH, E. J. & PERRIN, B. 2007*b* Transient buoyancy-driven front dynamics in nearly horizontal tubes. *Phys. Fluids* **19**, 123603.

TAGHAVI, S. M., ALBA, K., SEON, T., WIELAGE-BURCHARD, K., MARTINEZ, D. M. & FRIGAARD, I. A. 2012 Miscible displacement flows in near-horizontal ducts at low Atwood number. *J. Fluid Mech.* **696**, 175–214.

TAGHAVI, S. M., SEON, T., MARTINEZ, D. M. & FRIGAARD, I. A. 2009 Buoyancy-dominated displacement flows in near-horizontal channels: the viscous limit. *J. Fluid Mech.* **639**, 1–35.

TAGHAVI, S. M., SEON, T., MARTINEZ, D. M. & FRIGAARD, I. A. 2010 Influence of an imposed flow on the stability of a gravity current in a near horizontal duct. *Phys. Fluids* **22** (3), 031702.

TAGHAVI, S. M., SEON, T., WIELAGE-BURCHARD, K., MARTINEZ, D. M. & FRIGAARD, I. A. 2011 Stationary residual layers in buoyant Newtonian displacement flows. *Phys. Fluids* **23** (4), 044105.

TALON, L. & MEIBURG, E. 2011 Plane Poiseuille flow of miscible layers with different viscosities: instabilities in the Stokes flow regime. *J. Fluid Mech.* **686**, 484–506.

TAYLOR, G. I. 1953 Dispersion of soluble matter in solvent flowing slowly through a tube. *Proc. R. Soc. Lond.* A **219**, 186–203.

VANAPARTHY, S. H. & MEIBURG, E. 2008 Variable density and viscosity, miscible displacements in capillary tubes. *Eur. J. Mech. (*B/*Fluids* **27** (3), 268–289.

VEDERNIKOV, A., SCHEID, B., ISTASSE, E. & LEGROS, J. C. 2001 Viscous fingering in miscible liquids under microgravity conditions. *Phys. Fluids* **13** (9), S12.

WOODING, R. 1969 Growth of fingers at an unstable diffusing interface in a porous medium or Hele-Shaw cell. *J. Fluid Mech.* **39**, 477–495.

YIH, C. S. 1967 Instability due to viscosity stratification. *J. Fluid Mech.* **27**, 337.

YORTSOS, Y. C. & ZEYBEK, M. 1988 Dispersion driven instability in miscible displacement in porous media. *Phys. Fluids* **31**, 3511–3518.